Composite Weyl nodes stabilized by screw symmetry with and without time reversal

Stepan S. Tsirkin,[1, 2] Ivo Souza,[1, 3] and David Vanderbilt[4]
[1] *Centro de Física de Materiales, Universidad del País Vasco, 20018 San Sebastián, Spain*
[2] *Donostia International Physics Centre, 20018 San Sebastián, Spain*
[3] *Ikerbasque Foundation, 48013 Bilbao, Spain*
[4] *Department of Physics and Astronomy, Rutgers University, Piscataway, New Jersey 08854-8019, USA*
(Dated: April 1, 2017)

We classify the band degeneracies in three-dimensional crystals with screw symmetry n_m and broken $\mathcal{P} * \mathcal{T}$ symmetry, where $\mathcal{P}$ stands for spatial inversion and $\mathcal{T}$ for time reversal. The generic degeneracies along symmetry lines are Weyl nodes: Chiral contact points between pairs of bands. They can be single nodes with a chiral charge of magnitude $|\chi| = 1$ or composite nodes with $|\chi| = 2$ or 3, and the possible χ values only depend on the order n of the axis, not on the pitch m/n of the screw. Double Weyl nodes require $n = 4$ or 6, and triple nodes require $n = 6$. In all cases the bands split linearly along the axis, and for composite nodes the splitting is quadratic on the orthogonal plane. This is true for triple as well as double nodes, due to the presence in the effective two-band Hamiltonian of a nonchiral quadratic term that masks the chiral cubic dispersion. If $\mathcal{T}$ symmetry is present and $\mathcal{P}$ is broken there may exist on some symmetry lines Weyl nodes pinned to $\mathcal{T}$-invariant momenta, which in some cases are unavoidable. In the absence of other symmetries their classification depends on n, m, and the type of $\mathcal{T}$ symmetry. For spinless $\mathcal{T}$, such $\mathcal{T}$-invariant Weyl nodes are always double nodes; with spinful $\mathcal{T}$ they can be single or triple nodes, with the latter occurring not only on 6-fold axes but also on 3-fold ones. The in-plane band splitting of $\mathcal{T}$-invariant triple nodes is cubic, not quadratic as in the case of generic triple nodes. These rules are illustrated by means of first-principles calculations for hcp cobalt, a $\mathcal{T}$-broken, $\mathcal{P}$-invariant crystal with 6_3 symmetry, and trigonal tellurium, a $\mathcal{T}$-invariant, $\mathcal{P}$-broken crystal with 3-fold screw symmetry.

I. INTRODUCTION

The study of degeneracies in the energy spectrum of crystals has a long history in the band theory of solids. The early works focused on the consequences of symmetry [1–3], and it was only much later that the topological aspects of the problem began to be appreciated [4]. The interplay between topology and crystal symmetry can be particularly interesting. For example, Michel and Zak [5] used an argument based on the periodicity of reciprocal space to show that nonsymmorphic symmetries (screw axes and glide planes) necessarily lead to degeneracies on symmetry lines and planes in the Brillouin zone (BZ).

In recent years the study of band crossings has been reinvigorated by the discovery of gapless topological phases such as Weyl and Dirac semimetals, where the presence of degeneracies near the Fermi level can lead to striking observable effects [6]. A knowledge of the symmetry conditions under which certain types of degeneracies become possible, or even unavoidable, can greatly simplify the search and analysis of candidate materials.

Our focus here is on Weyl nodes, i.e., isolated twofold degeneracies that occur in three-dimensional (3D) band structures without having to fine-tune the Hamiltonian. In the simplest and most common case, the two bands split linearly in all directions away from the node [3]. Such contact points are the generic degeneracies in bulk crystals with broken $\mathcal{P} * \mathcal{T}$ symmetry, where $\mathcal{P}$ and $\mathcal{T}$ denote spatial inversion and time-reversal symmetry respectively. (If the combined $\mathcal{P} * \mathcal{T}$ symmetry is present, the bands are Kramers-degenerate everywhere in the BZ, and additional isolated degeneracies are known as Dirac nodes.) Weyl nodes are chiral, acting as monopole sources and sinks of Berry curvature in the BZ, and when the quantized Berry flux through some of the Fermi-surface sheets is nonzero the material is classified as a Weyl (semi)metal [6].

Weyl nodes are topologically protected by the discrete translational symmetry of the lattice (they can only be gapped by anihilating with other Weyl nodes of opposite chirality), and no further symmetries are needed for their existence. Nevertheless, the presence of other symmetries affects their location and characteristics. For example, 4-fold symmetry can stabilize Weyl nodes along a symmetry axis in the BZ, and in some cases the bands split quadratically in the directions perpendicular to the axis (but still linearly along the axis) [3, 7]. Such quadratic touchings may be regarded as consisting of two linear Weyl nodes of the same chirality brought together by rotational symmetry, and for that reason they are known as “double Weyl nodes” [7]. Furthermore, it has been shown that while point-group symmetry is not necessary, it can sometimes be sufficient to guarantee the existence of isolated band touchings at points of symmetry [8].

In this paper, we classify the band crossings occurring on the symmetry lines of 3D crystals with screw rotational symmetry and broken $\mathcal{P} * \mathcal{T}$ symmetry. We first describe the types of crossings that are possible at generic points along a symmetry line. We then specialize to $\mathcal{T}$-invariant, $\mathcal{P}$-broken crystals and consider the crossings at $\mathcal{T}$-invariant points on those lines, for both spinful and spinless $\mathcal{T}$ symmetry; the former applies to electrons in crystals, and the latter to the spectrum of photonic crystals [9], as well as to electronic bands calculated without including spin-orbit coupling. We find, for example, that in nonmagnetic crystals with a 3-fold screw axis Weyl nodes are unavoidable at the symmetry points Γ and A when spin-orbit is included. In a crystal like Te where the band structure is composed of 6-band complexes, each complex generates a triple Weyl node at Γ and another at A (in addition to two single Weyl nodes at each of those points). In contrast, the occurrence of triple nodes at generic points along a symmetry axis requires 6-fold symmetry [7]. The off-axis splitting of the bands in the orthogonal plane is qualitatively different in the two cases: It is cubic when the triple node is pinned to a $\mathcal{T}$-invariant point (either Γ or A) on a 3-fold or 6-fold axis, and quadratic when it occurs at a generic point along a 6-fold axis.

The article is organized as follows. In Sec. II we classify the Weyl nodes occuring at generic points along a rotation axis in the BZ. That section follows closely the discussion in Ref. [7] which we extend from pure rotations to screw rotations, and it also includes a new result on the in-plane dispersion of triple nodes. In. Sec. III we apply the classification scheme to Weyl nodes on the 6-fold axis in the BZ of ferromagnetic hcp Co. In Sec. IV we turn to nonmagnetic acentric crystals and classify the degeneracies occuring at $\mathcal{T}$-invariant momenta on a rotation axis. As an example, we study in Sec. V the Weyl nodes on the 3-fold axis in the BZ of trigonal Te, including the effect of a perturbation that breaks $\mathcal{T}$ symmetry but preserves the screw symmetry. The conclusions are drawn in Sec. VI, and some supplementary information and derivations are given in the appendices.

II. WEYL NODES AT GENERIC POINTS ALONG A ROTATION AXIS

In this section we consider the most general scenario in which Weyl points can occur along a symmetry line. Since their presence anywhere in the BZ requires broken $\mathcal{P} * \mathcal{T}$ symmetry, we assume this to be the case for our crystal. Examples include ferromagnetic metals such as body-centered cubic Fe [10] and hexagonal close-packed (hcp) Co, nonmagnetic acentric semiconductors such as trigonal Te [11, 12], and polar conductors such as TaAs, a Weyl semimetal [13, 14]. In the first two examples $\mathcal{T}$ symmetry is broken and $\mathcal{P}$ symmetry is present, while the reverse is true for the others. Note that certain antiferromagnets such as Cr_2O_3 do not qualify: They break $\mathcal{P}$ and $\mathcal{T}$ individually, but respect $\mathcal{P} * \mathcal{T}$.

We further assume that our crystal is left invariant under either a pure rotation or a screw operation $n'_{m'}$, where $n' = 2, 3, 4, 6$ denotes a counterclockwise $2\pi/n'$ rotation around the $+\hat{\mathbf{z}}$ axis, and the non-negative integer $m' < n'$ indicates a translation along $+\hat{\mathbf{z}}$ by a fraction m'/n' of the lattice constant c (which we take as the unit of length). If n is a divisor of n', invariance under $n'_{m'}$ implies invariance under n_m about the same axis, where $m = m'$ mod n. In the presence of n_m symmetry the Bloch Hamiltonian $H_{ij}(\boldsymbol{k}) = \langle \psi_{i\boldsymbol{k}} | H | \psi_{j\boldsymbol{k}} \rangle$ satisfies

$$C_{n_m} H(\boldsymbol{k}) C_{n_m}^{-1} = H(R_n \boldsymbol{k}), \tag{1}$$

where the matrix C_{n_m} represents the n_m operation in the Bloch basis and $R_n\boldsymbol{k}$ is the vector obtained by applying a counterclockwise rotation of $2\pi/n$ to $\boldsymbol{k}$. In writing Eq. (1) we have adopted the "active picture" where the action of a transformation S on a function $f(\boldsymbol{r})$ is described by $Sf(\boldsymbol{r}) = f(S^{-1}\boldsymbol{r})$.

We want to study the possible crossing between two eigenstates $|u\rangle$ and $|v\rangle$ of $H(\boldsymbol{k})$ along a rotationally-invariant line (a line where $R_n\boldsymbol{K} = \boldsymbol{K}$ mod $\boldsymbol{G}$ at every point $\boldsymbol{K}$). For clarity we will focus on the axis

$$\boldsymbol{K} = (0, 0, K_z) \tag{2}$$

that has the highest rotational symmetry $n = n'$, but our analysis also applies to the other invariant lines that are present in the BZ as a result of lattice periodicity. Henceforth we will use the symbol $\boldsymbol{K}$ to refer to a point with coordinates given by Eq. (2).

If the two states are very close in energy at $\boldsymbol{K}$ and comparatively far from other bands, we can work in the basis $|u\rangle = (1, 0)^T$ and $|v\rangle = (0, 1)^T$ choosing $|u\rangle$ as the higher-energy state at $K_z + \delta$ when $\delta \to 0^+$, and approximate the Bloch Hamiltonian around $\boldsymbol{K}$ by

$$H_{\text{eff}}(\boldsymbol{K} + \boldsymbol{q}) = d(\boldsymbol{q})\mathbb{1} + f(\boldsymbol{q})\sigma_+ + f^*(\boldsymbol{q})\sigma_- + g(\boldsymbol{q})\sigma_z, \tag{3}$$

where $\boldsymbol{q} = (q_x, q_y, q_z)$, $\mathbb{1}$ is the 2×2 identity matrix, $\sigma_\pm = \sigma_x \pm i\sigma_y$, and a dependence of the functions d, f, and g on $\boldsymbol{K}$ is implied. In this approximation the two basis states are eigenstates of $H_{\text{eff}}(\boldsymbol{K})$, which means that $f(\boldsymbol{q} = 0) = 0$. The condition for a crossing to occur at $\boldsymbol{K}$ is that $g(\boldsymbol{q} = 0) = 0$ as well, and in the following it is assumed we have found such a point. The functions f and g can then be expanded around $\boldsymbol{K}$ as

$$f(q_+, q_-, q_z) = \sum_{n_1 n_2 n_3} A_{n_1 n_2 n_3} q_+^{n_1} q_-^{n_2} q_z^{n_3}, \tag{4a}$$

$$g(q_+, q_-, q_z) = \sum_{m_1 m_2 m_3} B_{m_1 m_2 m_3} q_+^{m_1} q_-^{m_2} q_z^{m_3}, \tag{4b}$$

where $q_\pm = q_x \pm iq_y$, $A_{n_1 n_2 n_3}$ and $B_{m_1 m_2 m_3}$ are K_z-dependent complex coefficients with $n_i, m_i \geq 0$, and $A_{000} = B_{000} = 0$ by assumption. The requirement that Eq. (3) be Hermitian implies that $g(\boldsymbol{q})$ is real, leading to the relation

$$B_{m_1 m_2 m_3} = B^*_{m_2 m_1 m_3}. \tag{5}$$

The types of crossings that can occur at generic points along the axis, where n_m symmetry is present but $\mathcal{T}$ is broken, were classified in Ref. [7] by imposing the rotational constraint (1) on the effective Hamiltonian of Eqs. (3) and (4). The authors specialized to pure n-fold rotations ($m = 0$), and in the following we extend their treatement to include screw rotations. As we shall see, the resulting classification is independent of the pitch of the screw.

At any point along the axis Eq. (1) reduces to $[C_{n_m}, H(\boldsymbol{K})] = 0$, so that the energy eigenstates are also eigenstates of C_{n_m}. The rotational eigenvalues $\alpha(K_z)$ are determined by noting that $(n_m)^n$ describes a 2π rotation around the $+\hat{\mathbf{z}}$ axis followed (or preceeded) by a translation by $m\hat{\mathbf{z}}$. The former leaves a spinless wavefunction unchanged but flips the sign of a spinful wavefunction, and the latter gives an extra phase factor e^{-imK_z} (the minus sign comes from using the active picture). Taking the n-th roots we find

$$\alpha_p(K_z) = \gamma_{n_m}(K_z)\, e^{i2\pi p/n}, \tag{6a}$$

$$\gamma_{n_m}(K_z) = e^{i\pi(F-F'm)/n}, \tag{6b}$$

where p is an integer chosen between 0 and $n-1$, $F = 0$ ($F = 1$) for spinless (spinful) $\mathcal{T}$ symmetry, and $F' = K_z/\pi$. In the same basis of Eq. (3), then, the matrix describing the n_m operation reads

$$C_{n_m}(K_z) = \gamma_{n_m}(K_z) \begin{pmatrix} e^{i2\pi p_u/n} & 0 \\ 0 & e^{i2\pi p_v/n} \end{pmatrix}. \tag{7}$$

Combining Eqs. (1), (3), and (7) gives

$$e^{i\frac{2\pi}{n}(p_u-p_v)} f(q_+, q_-, q_z) = f\left(q_+ e^{i\frac{2\pi}{n}}, q_- e^{-i\frac{2\pi}{n}}, q_z\right), \tag{8a}$$

$$g(q_+, q_-, q_z) = g\left(q_+ e^{i\frac{2\pi}{n}}, q_- e^{-i\frac{2\pi}{n}}, q_z\right). \tag{8b}$$

Inserting Eq. (4a) in Eq. (8a) and Eq. (4b) in Eq. (8b) we find

$$n_1 - n_2 = p_u - p_v \mod n, \tag{9a}$$

$$m_1 - m_2 = 0 \mod n. \tag{9b}$$

The only nonzero elements of $A_{n_1 n_2 n_3}$ or $B_{m_1 m_2 m_3}$ occur when Eq. (9a) or (9b) is satisfied, respectively. When $p_u = p_v$ the degeneracy is nonchiral and can be gapped by a small perturbation that respects n_m symmetry (see Appendix A), whereas for $p_u \neq p_v$ it is chiral and robust.

We will use two criteria to classify the Weyl nodes that occur for $p_u \neq p_v$: (i) the power laws that describe at leading order the splitting of the bands as one moves away from the node along the axis and in the orthogonal directions, and (ii) the chiral charge of the node. Consider first the splitting of the bands. Regarding the behavior along the axis, the only surviving terms in Eqs. (4a) and (4b) when $q_+ = q_- = 0$ are those with $n_1 = n_2 = 0$ and $m_1 = m_2 = 0$ respectively. Then A_{00n_3} vanishes for all n_3 because of Eq. (9a), and to leading order in q_z we find

$$H_{\text{eff}}(0, 0, K_z + q_z) = B_{001}\sigma_z q_z. \tag{10}$$

From this we conclude that the band splitting is generically linear along the symmetry axis. With our choice of $|u\rangle = (1, 0)^T$ as the higher-energy state on the higher-K_z side of the crossing, B_{001} is positive [15].

TABLE I. Classification of Weyl nodes at generic points on an n-fold axis in the BZ of a crystal with n_m symmetry and broken $\mathcal{P}{*}\mathcal{T}$ symmetry. α_u and α_v are the rotational eigenvalues of the crossing states, with u denoting the higher-energy state on the higher-K_z side of the crossing. The Hamiltonian near a node on the plane perpendicular to the axis is $H_{\text{eff}}(q_x, q_y, K_z) = h_{\text{eff}} + h_{\text{eff}}^\dagger$, and $q_\pm = q_x \pm iq_y$. In each row the complex parameters a and b correspond to specific coefficients $A_{n_1 n_2 0}$ in Eq. (4a), and $c = B_{110}/2$ from Eq. (12) is real. χ is the chiral charge with $\chi_{ab} = \text{sgn}(|b| - |a|)$, and the off-axis band splitting at leading order is indicated as $q_\perp$ (linear) or $q_\perp^2$ (quadratic).

n	α_u/α_v	h_{eff}	χ	Splitting
2	-1	$(aq_+ + bq_-)\,\sigma_+$	χ_{ab}	$q_\perp$
3	$e^{\pm i2\pi/3}$	$aq_\pm\sigma_+$	∓1	$q_\perp$
4	$\pm i$	$aq_\pm\sigma_+$	∓1	$q_\perp$
4	-1	$c\left(q_x^2 + q_y^2\right)\sigma_z + \left(aq_+^2 + bq_-^2\right)\sigma_+$	$2\chi_{ab}$	$q_\perp^2$
6	$e^{\pm i\pi/3}$	$aq_\pm\sigma_+$	∓1	$q_\perp$
6	$e^{\pm 2i\pi/3}$	$c\left(q_x^2 + q_y^2\right)\sigma_z + aq_\pm^2\sigma_+$	∓2	$q_\perp^2$
6	-1	$c\left(q_x^2 + q_y^2\right)\sigma_z + \left(aq_+^3 + bq_-^3\right)\sigma_+$	$3\chi_{ab}$	$q_\perp^2$

The behavior on the orthogonal plane is described by $H_{\text{eff}}(q_x, q_y, K_z)$. We now need to collect the leading terms with $n_3 = 0$ in Eq. (4a) that satisfy condition (9a). Those terms determine the magnitude of the chiral charge, and their form only depends on n and on the ratio

$$\frac{\alpha_u}{\alpha_v} = e^{i2\pi(p_u-p_v)/n} \tag{11}$$

between the rotational eigenvalues of the crossing states. We must also collect terms with $m_3 = 0$ in Eq. (4b) that comply with condition (9b). At leading order we find $g(q_+, q_-, 0) = B_{110}q_+q_-$, or equivalently,

$$g(q_x, q_y, 0) = B_{110}(q_x^2 + q_y^2). \tag{12}$$

This term is allowed for all n, and it appears to have been overlooked in Ref. [7]. It does not affect the sign or magnitude of the chiral charge, but in some cases it qualitatively changes the off-axis band splitting. For triple nodes, in particular, this term dominates the band splitting in the plane normal to the axis, although a cubic splitting would still be evident if one could follow the parabolic $g(\boldsymbol{q}) = 0$ surface instead of the fixed-q_z plane.

By now we have gathered all the needed information to catalog the Weyl crossings that can occur at generic points on a rotation axis. The classification is given in Table I, and as anticipated it does not depend on the pitch m/n of the screw. The main conclusions are as follows. The occurrence of triple Weyl nodes requires 6-fold symmetry, double nodes require 4-fold or 6-fold symmetry, and rotation axes of any order can host single Weyl nodes. At leading order the band splitting along the axis is linear in all cases, while on the orthogonal plane it is linear for single nodes and quadratic for both double and triple nodes. These conclusions agree with Ref. [7], except for the realization that the in-plane splitting of a triple Weyl node is generally quadratic, not cubic. In Sec. IV we will encounter triple nodes for which the quadratic term (12) is disallowed by symmetry, resulting in a cubic in-plane dispersion.

III. APPLICATION TO HCP COBALT

In order to illustrate the preceeding discussion, we have performed an *ab-initio* study of the bandstructure of hcp Co. The technical details of the calculation are given in Appendix B. In the hcp structure (space group P6_3/mmc, No. 194), the c axis is a 6_3 screw axis. This is a "neutral screw" (a screw that has neither right or left sense [16]) that coexists with $\mathcal{P}$ symmetry, while $\mathcal{T}$ is broken by the ferromagnetic order. The spontaneous breaking of $\mathcal{T}$ symmetry occurs in the spin channel via the exchange interaction, and is then transmitted to the orbital wavefunctions and to the band structure by the spin-orbit interaction. In our calculation, the magnetization points along the positive haxagonal axis.

Figure 1(a) shows the energy bands near the Fermi level on a segment of the 6-fold axis ΓA. (For a more complete picture of the band structure of Co, see Ref. [17].) The different branches are color-coded by the rotational labels p in Eq. (6), which were determined directly from the Bloch wavefunctions. Already in this narrow energy range of ~ 0.8 eV one can find all the types of crossings listed in Table I for $n = 6$. For example, the crossing between the $p_u = 4$ and $p_v = 2$ branches near the bottom of the figure is a double Weyl node of negative chirality (chiral charge $\chi = -2$) because $\alpha_u/\alpha_v = e^{i2\pi/3}$, while the two crossings with $(p_u, p_v) = (2, 3)$ and $(3, 2)$ have $\chi = +1$ and $\chi = -1$, respectively. As expected, the crossing between the two branches with $p = 3$ is avoided. Triple Weyl nodes are generated at the crossings where $p_u - p_v = 3 \bmod 6$, namely $(p_u, p_v) = (0, 3)$ and $(4, 1)$; in this case the chirality sgn(χ) cannot be extracted from the symmetry labels. For each node, we have evaluated χ explicitly from the quantized Berry-curvature flux through a small enclosing box, as described in Appendix B. For the single and double nodes, the calculated values of χ agree in sign and magnitude with those predicted from the symmetry labels.

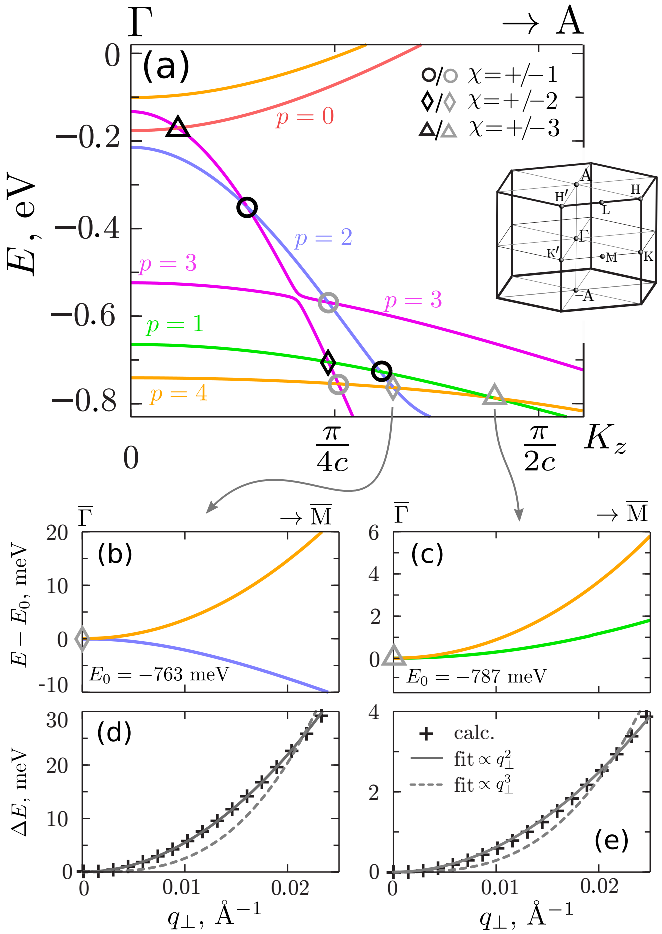

FIG. 1. (Color online) (a) Calculated band structure of hcp Co along the six-fold symmetry line ΓA. Energies are measured from the Fermi level, and each color denotes a branch labeled by the integer p in Eq. (6). Markers denote Weyl crossings with the indicated chiral charges χ. The inset shows the hexagonal BZ and its high-symmetry points. Panels (b) and (c) show the in-plane dispersions near a double and a triple Weyl node respectively, and panels (d) and (e) show the corresponding band splittings away from the nodes, together with the quadratic and cubic best fits.

Figure 1(a) confirms that the band dispersions along the axis are linear around every Weyl node. The dispersions are also linear in the transverse directions when $|\chi| = 1$ (not shown), but not when $|\chi| > 1$. Figures 1(b) and (c) show the dispersions near a double and a triple node respectively, along the in-plane direction $\overline{\Gamma\mathrm{M}}$ (denoted as $q_\perp$) on the constant-k_z plane of the node; in both cases, the in-plane dispersion is fairly isotropic near $q_\perp = 0$. Figures 1(d) and (e) show the band splittings with increasing $q_\perp$, together with their best fits by quadratic and cubic functions. The splitting at small $q_\perp$ is accurately described by $\propto q_\perp^2$ (rather than $\propto q_\perp^3$) for both the double *and* the triple node. This confirms that the in-plane dispersion of a triple node is dominated by the nonchiral quadratic term in Eq. (12), which masks the cubic dispersion from the chiral term $\left(A_{300}q_+^3 + A_{030}q_-^3\right)\sigma_+$ in the last row of Table I.

We are aware of one other work [18] where triple Weyl nodes at generic points on a 6-fold axis were studied numerically (for a haxagonal photonic crystal). That work only reports the band dispersions along the axis, which as expected are linear around each node (see Fig. 4 therein). The authors state that the in-plane dispersion is cubic for the triple nodes, but it is unclear whether this was verified numerically, or if it is simply a remark based on the conclusions of Ref. [7].

IV. WEYL NODES AT TIME-REVERSAL INVARIANT MOMENTA ON A ROTATION AXIS

A. Formal derivation

Let us resume the formal development of our systematic classification. In Sec. II we considered a broken-$\mathcal{P}*\mathcal{T}$ crystal with n_m symmetry, and classified the Weyl nodes occurring at generic points on the rotation axis of Eq. (2). For the remainder of this work we specialize to a $\mathcal{T}$-invariant, $\mathcal{P}$-broken crystal, and focus on points along that axis where $\mathcal{T}$ symmetry is present (the time-reversal invariant momenta, or TRIM). Since $\mathcal{T}$ maps $\boldsymbol{k}$ onto $-\boldsymbol{k}$ mod $\boldsymbol{G}$, such points occur at $K_z = 0$ and π, corresponding to $F' = 0$ and 1 respectively in Eq. (6). As for the additional symmetry lines not passing through Γ, they only contain TRIM if they are 2-fold or 4-fold axes [19].

We now find it more convenient to identify an eigenvalue of C_{n_m} by an index j via [compare with Eq. (6)]

$$\alpha_j = e^{i\pi j/n} \quad \text{where} \quad j = 2p + F - F'm, \tag{13}$$

so that the j are integers spaced two units apart. With this notation, $\mathcal{T}$ maps α_j into α_{-j}. If the two time-reversed states $|u\rangle$ and $|v\rangle = \mathcal{T}|u\rangle$ are distinct, they form a degenerate pair [20] to which we assign the labels $j_u = j$ and $j_v = -j$. We then wish to understand whether and how this pair splits as we move off the symmetry axis as described by Eqs. (3) and (4a), and to determine the monopole charge when the crossing is chiral. In this context, the results of the rotational symmetry analysis in Sec. II can be expressed via $p_u - p_v = (j_u - j_v)/2 = j$, so that the only nonzero elements of $A_{n_1 n_2 n_3}$ occur when

$$n_1 - n_2 = j \mod n, \tag{14}$$

while nonzero elements of $B_{m_1 m_2 m_3}$ must still comply with condition (9b).

Let us now turn to the conditions imposed by $\mathcal{T}$ itself, which are different depending on whether $F = 0$ or 1 because $\mathcal{T}^2 = (-1)^F$. The first thing to note is that unless the two time-reversed states have different rotational labels, when $F = 0$ they are actually the same state and there is no $\mathcal{T}$-protected degeneracy. Thus, we impose

$$j \neq 0, n \quad \text{when} \quad F = 0. \tag{15}$$

(From here on, j is chosen between 0 and $2n-1$.) When $F = 1$, the Kramers theorem guarantees that the two states are different [21] and the above restriction does not apply. These conclusions are in line with the “Wigner rules” for degeneracies in the presence of $\mathcal{T}$ symmetry [22].

$\mathcal{T}$ symmetry also imposes the restrictions

$$n_1 + n_2 + n_3 = F \mod 2, \tag{16a}$$

$$m_1 + m_2 + m_3 = 1 \mod 2 \tag{16b}$$

on the nonzero elements of $A_{n_1 n_2 n_3}$ and $B_{m_1 m_2 m_3}$, respectively. Both follow from the relation

$$\mathcal{T} H(\boldsymbol{k}) \mathcal{T}^{-1} = H(-\boldsymbol{k}). \tag{17}$$

To show this, let us express $\mathcal{T}$ in our basis by acting with it on a state $|w\rangle = a|u\rangle + b|v\rangle$. From $\mathcal{T}|v\rangle = (-1)^F|u\rangle$ and the antilinearity of $\mathcal{T}$ we obtain $\mathcal{T} = \sigma_x \mathcal{K}$ ($F = 0$) and $\mathcal{T} = -i\sigma_y \mathcal{K}$ ($F = 1$) with $\mathcal{K}$ the complex conjugation operator, so that $\mathcal{T} f(\boldsymbol{q}) \mathcal{T}^{-1} = f^*(\boldsymbol{q})$ and $\mathcal{T}\sigma_\pm\mathcal{T}^{-1} = (-1)^F \sigma_\mp$. Inserting Eq. (3) in Eq. (17) and using these identities gives $f(-\boldsymbol{q}) = (-1)^F f(\boldsymbol{q})$, which leads to Eq. (16a) when combined with Eq. (4a). Similarly, from $\mathcal{T} g(\boldsymbol{q}) \mathcal{T}^{-1} = g(\boldsymbol{q})$ and $\mathcal{T}\sigma_z\mathcal{T}^{-1} = -\sigma_z$ we get $g(-\boldsymbol{q}) = -g(\boldsymbol{q})$, which leads to Eq. (16b).

Armed with the above relations, we can proceed to classify the degeneracies at the TRIM $(0, 0, 0)$ and $(0, 0, \pi)$. We begin with the on-axis band splittings. As in Sec. II, we collect terms in Eq. (4b) with $m_1 = m_2 = 0$, excluding B_{000} which vanishes by assumption. Equation (9b) is automatically satisfied and Eq. (16b) forces m_3 to be odd, and so the leading term is generically

$$g(0, 0, q_z) = B_{001} q_z. \tag{18}$$

Turning to the expansion (4a) of $f(0, 0, q_z)$, we keep terms with $n_1 = n_2 = 0$ excluding A_{000}. Equation (14) requires $j = 0$ or n which conflicts with Eq. (15) when $F = 0$, and when $F = 1$ Eq. (16a) requires n_3 to be odd. Thus

$$f(0, 0, q_z) = \begin{cases} A_{001} q_z, & \text{when } F = 1 \text{ and } j = 0 \text{ or } n \\ 0, & \text{otherwise.} \end{cases} \tag{19}$$

In all cases $H_{\text{eff}}(0, 0, K_z + q_z)$ is linear in q_z, producing a linear band splitting along the axis.

In order to describe the in-plane behavior, let us collect the leading terms with $n_3 = 0$ in Eq. (4a). Equation (16a) can then be written as

$$n_1 - n_2 = F \mod 2, \tag{20}$$

which together with Eqs. (14) and (15) constrains the form of $f(q_+, q_-, 0)$. Turning to $g(q_+, q_-, 0)$ and setting $m_3 = 0$ in Eq. (16b) we conclude that $m_1 - m_2$ must be odd, which excludes terms with $m_1 = m_2$ such as Eq. (12). The requirement that $m_1 - m_2$ be odd conflicts with condition (9b) when n is even, and so we find

$$g(q_+, q_-, 0) = \begin{cases} 2\text{Re}\left(B_{300} q_+^3\right), & \text{for } n = 3 \\ 0, & \text{for } n = 2, 4, 6. \end{cases} \tag{21}$$

In summary, the band splitting moving away from a degeneracy protected by $\mathcal{T}$ and n_m symmetry at $K_z = 0$ or π is generically linear along the axis. Assuming no other symmetries, the form of the in-plane Hamiltonian $H_{\text{eff}}(q_+, q_-, K_z)$ is constrained by Eqs. (14), (15), (20), and (21); the type of $\mathcal{T}$ symmetry (F) enters the first three equations, and an additional dependence on the pitch m/n is introduced by Eqs. (14) and (15) at $K_z = \pi$. The Weyl-like solutions compatible with lattice periodicity are listed in Table II for spinless $\mathcal{T}$, and in Table III for spinful $\mathcal{T}$. With spinless $\mathcal{T}$ all Weyl degeneracies are double nodes, and with spinful $\mathcal{T}$ they are either single

TABLE II. Classification of spinless Weyl nodes at the TRIM $K_z = 0$ and π on an n-fold axis in the BZ of a crystal with n_m and $\mathcal{T}$ symmetries. Each row is uniquely identified by the values of n and of the symmetry label j defined in Eq. (13), from which the remaining columns can be generated. The values of m for which the given j occurs at $K_z = 0$ and π are listed under $m(0)$ and $m(\pi)$, respectively, and the rest of the notation is as in Table I.

n	$m(0)$	$m(\pi)$	j	h_{eff}	χ	Splitting
3	—	1	1	$aq_-^2\sigma_+$	$+2$	$q_\perp^2$
3	all	0,2	2	$aq_+^2\sigma_+$	-2	$q_\perp^2$
3	all	0,2	4	$aq_-^2\sigma_+$	$+2$	$q_\perp^2$
3	—	1	5	$aq_+^2\sigma_+$	-2	$q_\perp^2$
4	all	0,2	2	$\left(aq_+^2 + bq_-^2\right)\sigma_+$	$2\chi_{ab}$	$q_\perp^2$
4	all	0,2	6	$\left(aq_+^2 + bq_-^2\right)\sigma_+$	$2\chi_{ab}$	$q_\perp^2$
6	all	0,2,4	2	$aq_+^2\sigma_+$	-2	$q_\perp^2$
6	all	0,2,4	4	$aq_-^2\sigma_+$	$+2$	$q_\perp^2$
6	all	0,2,4	8	$aq_+^2\sigma_+$	-2	$q_\perp^2$
6	all	0,2,4	10	$aq_-^2\sigma_+$	$+2$	$q_\perp^2$

TABLE III. Classification of spinful Weyl nodes at the TRIM $K_z = 0$ and π on an n-fold axis in the BZ of a crystal with n_m and $\mathcal{T}$ symmetries. The notation is the same as in Tables I and II, except that $c = B_{300}$ is a complex coefficient.

n	$m(0)$	$m(\pi)$	j	h_{eff}	χ	Splitting
2	all	0	1	$aq_-\sigma_+$	$+1$	$q_\perp$
2	all	0	3	$aq_+\sigma_+$	-1	$q_\perp$
3	—	1	0	$\left(aq_+^3 + bq_-^3\right)\sigma_+ + cq_+^3\sigma_z$	$3\chi_{ab}$	$q_\perp^3$
3	all	0,2	1	$aq_+\sigma_+$	-1	$q_\perp$
3	—	1	2	$aq_-\sigma_+$	$+1$	$q_\perp$
3	all	0,2	3	$\left(aq_+^3 + bq_-^3\right)\sigma_+ + cq_+^3\sigma_z$	$3\chi_{ab}$	$q_\perp^3$
3	—	1	4	$aq_+\sigma_+$	-1	$q_\perp$
3	all	0,2	5	$aq_-\sigma_+$	$+1$	$q_\perp$
4	all	0,2	1	$aq_+\sigma_+$	-1	$q_\perp$
4	all	0,2	3	$aq_-\sigma_+$	$+1$	$q_\perp$
4	all	0,2	5	$aq_+\sigma_+$	-1	$q_\perp$
4	all	0,2	7	$aq_-\sigma_+$	$+1$	$q_\perp$
6	all	0,2,4	1	$aq_+\sigma_+$	-1	$q_\perp$
6	all	0,2,4	3	$\left(aq_+^3 + bq_-^3\right)\sigma_+$	$3\chi_{ab}$	$q_\perp^3$
6	all	0,2,4	5	$aq_-\sigma_+$	$+1$	$q_\perp$
6	all	0,2,4	7	$aq_+\sigma_+$	-1	$q_\perp$
6	all	0,2,4	9	$\left(aq_+^3 + bq_-^3\right)\sigma_+$	$3\chi_{ab}$	$q_\perp^3$
6 B	all	0,2,4	11	$aq_-\sigma_+$	$+1$	$q_\perp$

or triple nodes. Triple nodes occur not only for $n = 6$ as in Table I but also for $n = 3$, and in both cases the in-plane splitting is cubic, not quadratic as in Table I.

B. Schematic description: (F, n_m) diagrams

Let us illustrate the use of Tables II and III by considering some specific combinations (F, n_m). We start with $(0, 3_1)$, i.e., spinless $\mathcal{T}$ and a right-handed 3-fold screw. At $K_z = 0$ along a 3_1-invariant axis the states carry labels $j = 0, 2, 4$ [Eq. (13)]. The $j = 0$ states are nondegenerate [Eq. (15)], while time-reversed pairs of states with labels $(j, -j + 2n) = (2, 4)$ or (4,2) form double Weyl nodes of negative or positive chirality respectively (second and third rows of Table II). At $K_z = \pi$ the possible labels are $j = 1, 3, 5$; the $j = 3$ states are nondegenerate, and the pairs (1,5) and (5,1) form double Weyl nodes of positive and negative chirality respectively. As K_z goes from 0 to π the rotational eigenvalues of Eq. (13) wind as $e^{-iK_z/3}$, so that $j = 0$ goes into $j = 5$, $j = 2$ into $j = 1$, and $j = 4$ into $j = 3$. Except for the chiralities, all this information is presented schematically in Fig. 2(a).

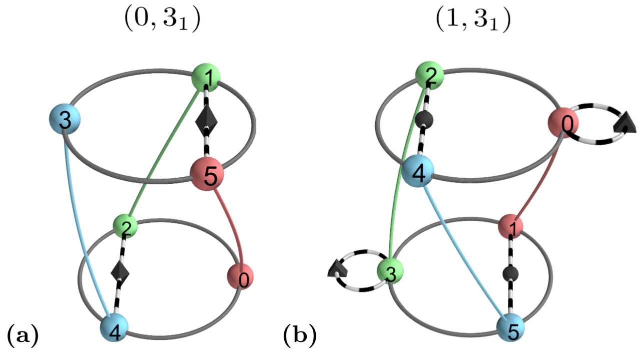

FIG. 2. (Color online) Schematic representation of the degeneracies at the TRIM along a 3_1-invariant axis. Panel (a) is for spinless $\mathcal{T}$ ($F = 0$), and panel (b) for spinful $\mathcal{T}$ ($F = 1$). Solid gray circles represent the complex unit circle, with the rotational eigenvalues of Eq. (13) at $K_z = 0$ (bottom) and $K_z = \pi$ (top) marked as spheres labeled by j, and their windings with K_z represented by lines with matching colors. A dashed line or loop connecting spheres indicates that a pair of time-reversed states with those labels forms a single (●), double (♦), or triple (▲) Weyl node.

Figure 2(b) shows the $(1, 3_1)$ diagram, where the allowed j values have shifted by $+1$ compared to Fig. 2(a). With spinful $\mathcal{T}$ the restriction (15) does not apply, and all bands pair up to form either single or triple Weyl nodes at both $K_z = 0$ and π. The triple nodes are formed between Kramers pairs with the same label $j = 0$ or $j = 3$ located on the equator of the unit circle.

Consider now the $(0, 2_1)$ diagram in Fig. 3(a). The symmetry labels at $K_z = 0$ are $j = 0, 2$. Since $F = 0$ and these labels lie on the equator, the states are nondegenerate; this explains their absence from Table II. At $K_z = \pi$ the labels are $j = 1, 3$, and they also do not appear in Table II (where there are no entries with $n = 2$) even though such states must be pairwise degenerate according to the Wigner rules. The reason is that the degeneracy is not an isolated Weyl node. Instead, the bands remain glued together over the entire BZ face [2, 22]. A dashed line without a marker is used to represent this nonchiral "sticking of the bands."

The $(1, 2_1)$ diagram of Fig. 3(b) shows that with spinful

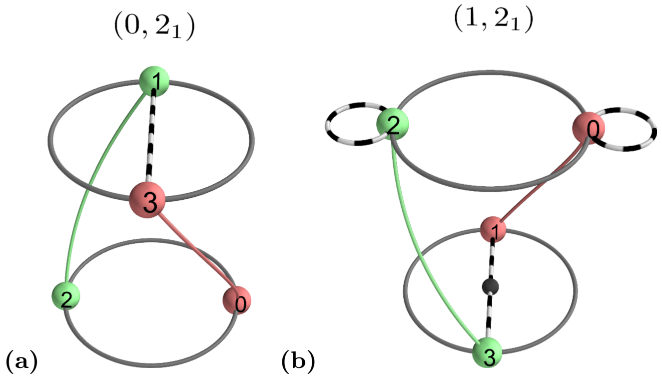

FIG. 3. (Color online) Same as Fig. 2, but for a 2_1-invariant axis. Dashed-line connectors without a marker in the middle represent nonchiral degeneracies caused by band-glueing across the BZ face orthogonal to the symmetry axis.

$\mathcal{T}$ all bands pair up to form single Weyl nodes at $K_z = 0$. The bands are again glued together over the entire BZ face at $k_z = \pi$, but now the degenerate partners share the same label, $j = 0$ or 2, on the rotation axis.

Band-glueing across a BZ face orthogonal to a 2_1 axis occurs in $\mathcal{T}$-invariant crystals because points on the BZ face are mapped onto themselves by $\mathcal{T} * 2_1$; the fact that this symmetry operation is antiunitary and squares to -1 (for both $F = 0$ and $F = 1$) then forces a Kramers degeneracy [21]. Since the presence of either 4_1, 4_3, 6_1, 6_3 or 6_5 symmetry implies the presence of 2_1 symmetry, the band sticking occurs for all of them. Indeed, one can see that Eqs. (14) and (20) require $F'm$ to be even when n is even. As a result, $f(q_+, q_-, 0)$ vanishes when n is even, m odd, and $K_z = \pi$. Together with Eq. (21), this implies that when n is even and m is odd the dispersion on the $k_z = \pi$ plane is described by $H_{\text{eff}}(q_x, q_y, \pi) = d(q_x, q_y, 0)\mathbb{1}$, confirming that the bands remain glued together across the BZ face. The combination of $\mathcal{T}$ with screw symmetries other than the ones listed above (i.e, with 3_1, 3_2, 4_2, 6_2, or 6_4) does not provoke band-glueing and can stabilize Weyl nodes at $K_z = \pi$, as we already saw for 3_1.

The complete set of (F, n_m) diagrams is given in the Appendix C. A few special cases of our systematic classification have been noted in the recent literature. Double Weyl nodes protected by 3_0 and spinless $\mathcal{T}$ symmetry [see the $(0, 3_0)$ diagram in Appendix C] were treated in Ref. [18], and triple nodes protected by 6-fold symmetry and spinful $\mathcal{T}$ symmetry are mentioned in Ref. [23].

V. APPLICATION TO TRIGONAL TELLURIUM

Elemental Te is a nonmagnetic semiconductor that crystalizes in two enantiomorphic structures with space groups P$3_1$21 (No. 152, right-handed) and P$3_2$21 (No. 154, left-handed). The unit cell contains three atoms disposed along a spiral chain, with the chains arranged on a hexagonal net. The structure and its symmetries are detailed in Refs. [24, 25], where it can be seen that the spiral chains reduce the symmetry from hexagonal to trigonal. In the following we pick right-handed Te and classify the Weyl crossings along the trigonal axis ΓA in the hexagonal BZ shown in Fig. 1(a). (For left-handed Te the band structure is identical, but the chiral charges flip sign.)

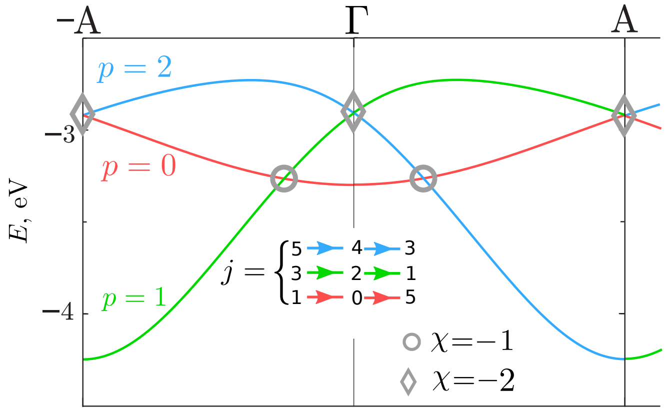

FIG. 4. (Color online) A connected group of three valence bands in trigonal tellurium along the rotationally-invariant line ΓA, calculated without including spin-orbit coupling. Energies are measured from the valence-band maximum, and each color denotes a branch labeled by the integer p in Eq. (6). For each branch, the values of the label j in Eq. (13) at −A, Γ and A (respectively, $K_z = -\pi, 0$ and π) are also indicated. Markers denote Weyl crossings with chiral charges χ.

The valence-band maximum and conduction-band minimum of trigonal Te occur close to the H point on the HK line. Without spin-orbit coupling the conduction-band minimum is exactly at H, and with spin-orbit the topmost valence band has a "camelback" shape, with a local minimum at H and two maxima at either side of H along HK [26]. States along the ΓA line are far from the band edges and hence do not participate in the low-energy physics. We will study them with the sole purpose of illustrating our classification scheme for Weyl nodes.

A. Spinless bands

We begin with a calculation that does not include spin-orbit coupling. The bands split into "elementary representations" [5] containing three bands each, and in Fig. 4 we plot along ΓA the second-highest valence-band complex. As in Fig. 1, each color denotes a branch labeled by the integer p in Eq. (6), with the branch cuts chosen at $K_z = \pi \bmod 2\pi$. The labels were determined in two ways: (i) by direct calculation starting from the wavefunctions, and (ii) using $p = j(\Gamma)/2$ [Eq. (13)], after determining the j labels at Γ and A as explained below.

It can be seen from Eq. (6) that as K_z changes by 2π, branch p connects with branch $p - m \bmod n$, which in the present case amounts to $p-1 \bmod 3$. This is the monodromy phenomenom described in Ref. [5], and it implies that the three bands must be connected along the ΓA line in such a way that one can travel continuously through all of them. The argument only relies on screw symmetry and is silent on the nature and location of the contact points, which also depend on the $\mathcal{T}$ symmetry [5].

Let us first classify the degeneracies at Γ and A in Fig. 4, with the help of the $(0, 3_1)$ diagram in Fig. 2(a). The band that is nondegenerate at Γ has $j=0$, and the two degenerate bands have $j=2$ and 4. The $j=4$ state evolves to become the nondegenerate $j=3$ state at A, while $j=2$ evolves into $j=1$ to become degenerate with the $j=5$ state which evolved from $j=0$. The two degenerate pairs, one at Γ and one at A, form double Weyl nodes. By consulting Table II we conclude that both have negative chirality [for the node at Γ (A), the higher-energy state at $K_z=0^+$ ($K_z=\pi^+$) has label $j=2$ ($j=5$)]. As in Sec. III we have checked these results by calculating the chiral charges explicitly from the Berry curvature, and the same was done for the other cases discussed below.

We have been assuming that the only symmetries present at Γ and A are 3_1 and $\mathcal{T}$, when in fact those points are also left invariant under 2-fold rotations along the ΓK and AH axes respectively [24, 25]. This does not change our conclusions, because the presence of 2_0 symmetry does not lead to degeneracies at either Γ or A, as can be seen from the $(0, 2_0)$ diagram in Fig. 7 of Appendix C. Hence, the degeneracies that do occur at those symmetry points are correctly described by the $(0, 3_1)$ diagram.

Let us now determine the chiral charges of the two non-TRIM crossings in Fig. 4; since they are related by a 2-fold rotation it is sufficient to focus on one of them, e.g., that between the red and blue branches on the right-hand side of the figure. Recalling that $|u\rangle$ and $|v\rangle$ are respectively the higher- and lower-energy states after the crossing, we assign $p_u=0$ and $p_v=2$. Equation (11) then gives $\alpha_u/\alpha_v=e^{i2\pi/3}$, and consulting Table I we find $\chi=-1$, in agreement with the calculated value.

In this particular example, it was possible to characterize all the contact points on the symmetry axis without having to calculate explicitly from the wavefunctions either their chiral charges or the rotational symmetry labels of the crossing bands. While the crossings at Γ and A are topologically required by the monodromy argument, those at intermediate K_z values can be eliminated by changing the Hamiltonian without changing the symmetry [5]. This is discussed further in Appendix D.

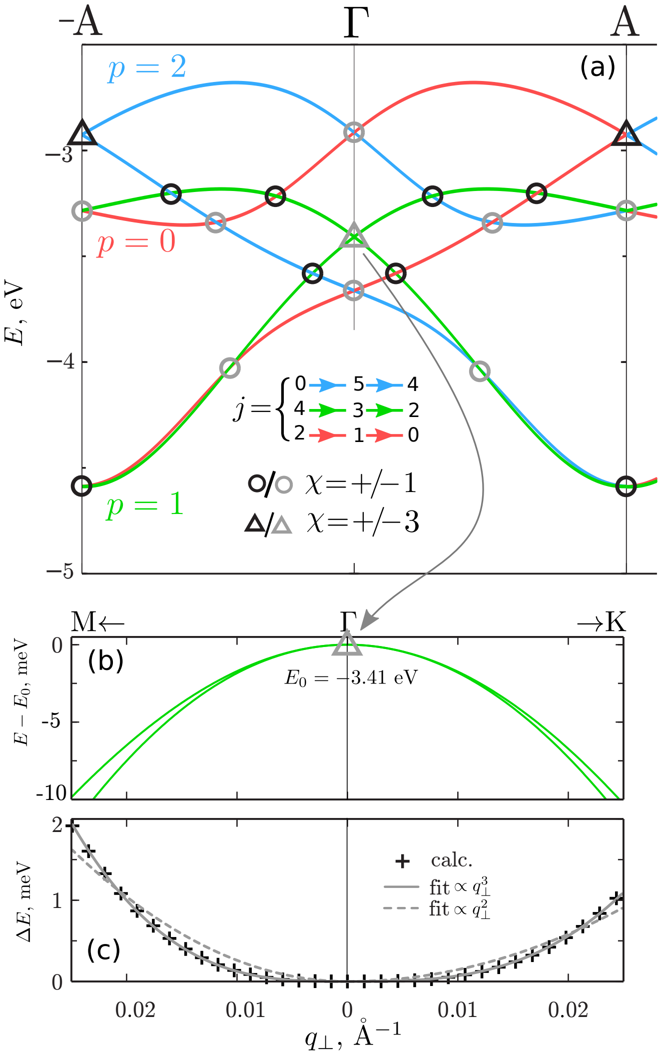

FIG. 5. (Color online) (a) Same as Fig. 4 but with spin-orbit coupling included, resulting in a connected group of six bands. (b) Off-axis dispersion near the triple Weyl point at Γ. (c) The corresponding splitting of the bands, together with its cubic and quadratic best fits. The band splittings along the ΓM and ΓK directions were fitted separately.

B. Spinful bands

Upon inclusion of spin-orbit coupling the 3-band complex of Fig. 4 turns into the 6-band complex of Fig. 5(a). The branches are color-coded by the symmetry labels $p=0,1,2$ in the same way as in Fig. 4, with two branches for each p. Let us label the bands, ordered in energy at each $\boldsymbol{k}$, from one to six. If we start at −A on the sixth band and follow the topmost $p=2$ branch from $K_z=-\pi$ to $K_z=\pi$, it connects with the fourth band on a $p=1$ branch. After one more monodromy cycle that branch connects with the the second band at −A on a $p=0$ branch, which connects back with the original $p=2$ branch on the sixth band after a third cycle. So far we have only covered half of the band complex; in order to span the other half (comprising three more branches with $p=0,1,2$), we can carry out a new sequence of monodromy cycles starting from the fifth band at −A. Each band is split in half between the two groups of three branches, and the two groups are connected to one another by the continuity in $\boldsymbol{k}$ of energy bands.

As in the spinless case, the qualtitative features of the degeneracies at Γ and A can be inferred by simply inspecting the band structure and referring to the corresponding diagram in Fig. 2(b). According to that diagram, Weyl nodes are unavoidable at both points; since all allowed j labels occur the same number of times within the complex, at each TRIM two of the nodes must be single Weyl nodes and one a triple node. Note also that states forming the triple node at one TRIM must hook up with states belonging to different single nodes at the other. It is then sufficient, in order to label all six bands, to identify one of the triple nodes (e.g., by examining the in-plane band splittings and selecting the one that is nonlinear). Suppose we have established that the triple node at Γ is the middle one in energy, as indicated in the figure. Since it connects with the two lower-energy nodes at A, these must be single nodes; as expected, the remaining (triple) node at A connects with the two single nodes at Γ. We can now assign all the j labels at Γ and A, and Table III then gives the chiralities of all four single nodes at those two points (but not of the two triple nodes, whose chiralities are not fixed by the symmetry labels and had to be determined from the Berry flux).

Figures 5(b) and 5(c) show the in-plane dispersion and splitting of the bands around the triple Weyl node at Γ. In this case the splitting is cubic as predicted in Sec. IV A, not quadratic as for triple nodes occuring at generic points along a 6-fold axis [e.g., Fig. 1(e)].

Finally, consulting Table I we find the chiralities of the five band crossings between Γ and A in Fig. 5, which must be single Weyl nodes since the axis has 3-fold symmetry. Amusingly, the rules for determining the chiralities in this case are those of the game "Rock–paper–scissors"[27]: A red branch is "rock," blue is "paper," and green is "scissors." If the higher-energy state after the crossing is the winner then $\chi = +1$, otherwise $\chi = -1$; since branches of the same color do not cross, there can be no tie. In Appendix D we repeat the above analysis for two more 6-band complexes in the spinor band structure of Te.

In closing, we mention that Weyl nodes in the spinor band structure of Te were studied in Refs. [11, 12]. The main focus of both works was on the nodes occuring close to the valence-band maximum and conduction-band minimum near the H point. The existence of triple Weyl nodes at Γ and A is not mentioned in either work, where all the reported Weyl points have $|\chi| = 1$.

C. Effect of a $\mathcal{T}$-breaking perturbation

In this section we study how the Weyl nodes located on the ΓA line are effected by a perturbation that breaks $\mathcal{T}$ symmetry but preserves the 3_1 symmetry of Te. For this purpose we recalculate the spinor band structure in the presence of a weak local Zeeman field directed along the trigonal axis, which induces a finite magnetic moment $\boldsymbol{\mu} = \mu_z \hat{\mathbf{z}}$ on each Te atom. Technically this is achieved by adding a "penalty term" of the form $\lambda \sum_{i=1}^{3} |\boldsymbol{\mu} - \boldsymbol{\mu}_i|^2$ to the density functional during the self-consistent loop. Here $\boldsymbol{\mu}_i$ is the self-consistent magnetic moment on the i-th atom in the unit cell, and $\lambda > 0$ is an adjustable parameter.

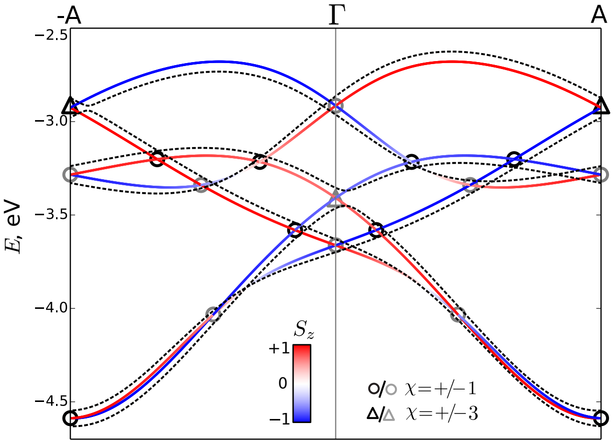

FIG. 6. Solid lines: Ground-state band structure of Te color-coded by the expectation value of the spin (in units of $\hbar/2$) projected along the trigonal axis $\hat{\mathbf{z}}$. Dashed lines: The band structure in the presence of a macroscopic magnetization amounting to a magnetic moment per atom of $\mu_z = 0.01\mu_{\mathrm{B}}$. Symbols denote Weyl nodes in the ground state with $\boldsymbol{\mu} = 0$, and energies are measured from the ground-state valence-band maximum.

To lowest order, the contribution of the induced magnetization to the Hamiltonian takes the form

$$\Delta H \propto M_z \tau_z \tag{22}$$

in the basis of the unperturbated eigenstates. Here M_z is the magnetization and τ_z is the Pauli matrix describing the spin degree of freedom, not to be confused with the pseudospin matrix σ_z in Eq. (3). Since our discussion will be qualitative, we are content to leave Eq. (22) expressed as a proportionality.

Figure 6 shows how the band structure on the ΓA line changes in the presence of a small positive M_z. The "generic" Weyl nodes away from Γ and A, which are pinned to the symmetry axis by the 3_1 symmetry, remain on the axis because that symmetry is preserved with $\boldsymbol{M} \parallel \hat{\mathbf{z}}$. However, they move in energy and wavevector, in a way that depends on the spin projections of the two crossing states. This behavior can be understood from the effective 2-band Hamiltonian near a generic Weyl node of charge $\chi = \mp 1$, which reads

$$H_{\text{eff}}(q_+, q_-, q_z) = \begin{pmatrix} \alpha q_z + M_z s_u & 2a q_\pm \\ 2a^* q_\mp & -\alpha q_z + M_z s_v \end{pmatrix} \tag{23}$$

with the zero of energy placed at the unperturbed crossing. Here $s_u = \langle u|\tau_z|u\rangle$ and $s_v = \langle v|\tau_z|v\rangle$ are the spin projections of the upper- and lower-energy states on the right-hand side of the crossing. Note that the perturbation (22) does not introduce off-diagonal terms in the effective Hamiltonian: Since $p_u \neq p_v$ for single Weyl nodes,

$\langle u|\tau_z|v\rangle$ vanishes according to Appendix A. For $M_z = 0$ and $q_z = 0$ Eq. (23) reduces to the Hamiltonian given in the second row of Table I; for $M_z = 0$ and $q_+ = q_- = 0$ it reduces to Eq. (10), with the positive coefficient B_{001} written here as α.

Assuming the crossing states are the eigenstates of the spin projection S_z (implying $|s_u| = |s_v| = 1$), we can derive from Eq. (23) with $q_+ = q_- = 0$ the following rules for how generic Weyl nodes on the ΓA line shift under a small positive M_z:

$\mathrm{sgn}(s_u)$	$\mathrm{sgn}(s_v)$	direction of shift
$+$	$+$	to higher energy
$-$	$-$	to lower energy
$+$	$-$	to lower K_z
$-$	$+$	to higher K_z

Even though the crossing states are generally not eigenstates of S_z, these simple rules describe fairly well the shifts of most of generic nodes in Fig. 6.

Let us turn now to the Weyl nodes pinned to Γ and A by $\mathcal{T}$ symmetry. In this case the unpreturbed crossing states are time-reversal partners, so that $s_v = -s_u$. Consider first the nodes with $|\chi| = 1$. When $\mathcal{T}$ is broken by M_z, those nodes move away from the TRIM but remain on the ΓA axis by virtue of the unbroken 3_1 symmetry, and their motion along the axis obeys the same rules discussed above for the generic single Weyl nodes. Note that the positive node at A and ~ -4.5 eV moves to the left and anihilates with the negative node at ~ -4.0 eV and halfway between Γ and A, which moves to the right.

The most striking effect of the axial Zeeman field is on the triple Weyl nodes at Γ and A. In Fig. 6, gaps open up near those nodes when $M_z \neq 0$. That happens because $\mathcal{T}$ symmetry not only pins those nodes to the TRIM, but is essential for their existence on a 3-fold axis (recall that without $\mathcal{T}$ symmetry, triple nodes can only occur on 6-fold axes). Once the $\mathcal{T}$ symmetry is broken, each triple node splits into three single nodes; these are not visible in Fig. 6 because they are located off the ΓA axes on ΓMLA planes (see below).

In order to understand the splitting pattern, let us write the effective Hamiltonian for a triple node including the perturbing term (22). Taking the unperturbed terms with $q_z = 0$ from the third row in Table III and the unperturbed terms with $q_+ = q_- = 0$ from Eq. (19) we find, setting $A_{001} = \beta$ and using $s_v = -s_u$,

$$\begin{aligned} H_{\text{eff}}(q_+, q_-, q_z) = {} & (\alpha q_z + c q_+^3 + c^* q_-^3 + s_u M_z)\sigma_z + \\ & \left[(a q_+^3 + b q_-^3 + \beta q_z + \gamma M_z)\sigma_+ + \text{H.c.}\right], \end{aligned} \tag{24}$$

where $\gamma = \frac{1}{2}\langle u|\tau_z|v\rangle$ and "H.c." stands for Hermitian conjugate. Without additional symmetries all coefficients here are generally complex, except for α which is real and positive. The condition for a degeneracy to occur is that the prefactors of the σ_z and $\sigma_\pm$ matrices should vanish simultaneously. Thus

$$q_z = -\frac{1}{\alpha}(s_u M_z + c q_+^3 + c^* q_-^3), \tag{25}$$

which inserted into the prefactor of σ_+ gives

$$\widetilde{a} q_+^3 + \widetilde{b} q_-^3 + \widetilde{\gamma} M_z = 0, \tag{26}$$

where $\widetilde{a} = a - c\beta/\alpha$, $\widetilde{b} = b - c^*\beta/\alpha$ and $\widetilde{\gamma} = \gamma - \beta s_u/\alpha$. Writing $q_\pm$ as $q_\perp e^{\pm i\phi}$ with $q_\perp > 0$ leads to

$$q_\perp^3(\widetilde{a} e^{i3\phi} + \widetilde{b} e^{-i3\phi}) + \widetilde{\gamma} M_z = 0. \tag{27}$$

The condition $\arg(\widetilde{a} e^{i3\phi} + \widetilde{b} e^{-i3\phi}) = \arg(-\widetilde{\gamma} M_z)$ for the phase has three roots separated by $2\pi/3$. This means that the in-plane splitting pattern of a triple node respects 3-fold symmetry, as expected. For the magnitude of the splitting we get

$$q_\perp^3 = \left| \frac{\widetilde{\gamma} M_z}{\widetilde{a} e^{i3\phi} + \widetilde{b} e^{-i3\phi}} \right|. \tag{28}$$

Thus the in-plane splitting increases as $|M_z|^{1/3}$, and from Eq. (25) we conclude that the vertical shift of the three split nodes is instead linear in $|M_z|$. However, unlike for a single Weyl node, the direction of the on-axis shift of a triple node in not uniquely defined by the spin projections of the crossing states, but depends on microscopic parameters.

The previous analysis correctly predicts a 3-fold symmetric in-plane splitting of a $\mathcal{T}$-invariant triple node on a 3-fold axis, but it does not determine its absolute orientation. In order to do so it is necessariy to take into consideration an additional symmetry of trigonal Te, namely the two-fold rotation. In Appendix E we show that this symmetry pins the three split Weyl nodes to the ΓMLA planes, as confirmed by the first-principles calculations.

In the case of a $\mathcal{T}$-invariant triple node on a 6-fold axis, the effect of an axial Zeeman field would have been quite different. Instead of splitting into three single nodes the triple node would simply move away from the TRIM along the axis, and its in-plane dispersion would change from cubic to quadratic.

VI. CONCLUSIONS

We have carried out a systematic classification of the types of degeneracies that can occur on symmetry lines in the BZ of a 3D crystal with pure rotational or screw symmetry n_m, assuming broken $\mathcal{P} * \mathcal{T}$ symmetry and in the absence of other crystallographic symmetries. We first presented the classification for the generic case, and then specialized to $\mathcal{T}$-invariant, $\mathcal{P}$-broken crystals, treating both spinless and spinful $\mathcal{T}$. At generic points along a symmetry axis the degeneracies are Weyl nodes. At $\mathcal{T}$-invariant points on an axis they can be either Weyl nodes or, when n is even and m is odd, glueing of pairs of bands extending over the entire perpendicular BZ face.

It was known from previous work [7] that the presence of either 4-fold or 6-fold rotational symmetry without $\mathcal{T}$ symmetry can stabilize Weyl nodes with a chiral charge of magnitude larger than one, namely $|\chi| = 2$ when $n = 4$ or 6 and also $|\chi| = 3$ when $n = 6$. In this work we have found a new type of triple Weyl node that can occur in crystals with spinful $\mathcal{T}$ symmetry and any of the following symmetries: $3_0, 3_1, 3_2, 6_0, 6_2, 6_4$. The two types are qualitatively different: Generic triple nodes protected by 6-fold symmetry alone are *dressed*, with the in-plane cubic chiral dispersion masked by a nonchiral quadratic dispersion that dominates the band splitting; thus, at leading order the band splitting is indistinguishable from that of a double node. Instead, $\mathcal{T}$-invariant triple nodes on a 3-fold or a 6-fold axis are *naked*, displaying a purely cubic in-plane splitting. This means that there is no one-to-one correspondance between the chiral charge of a Weyl node on a symmetry axis and the leading-order in-plane splitting of the bands. Hexagonal close-packed Co and trigonal Te are examples of materials possessing dressed and naked triple Weyl nodes, respectively.

In summary, we have shown that composite Weyl nodes are more common and more diverse than previously thought, and that in some cases they are unavoidable. We hope that these findings will stimulate the search for new classes of Weyl semimetals where $\mathcal{T}$-invariant Weyl nodes on symmetry axes occur close to the Fermi level.

ACKNOWLEDGMENTS

S.S.T and I.S. acknowledge support from Grant No. FIS2016-77188-P from the Spanish Ministerio de Economía y Competitividad, Grant No. CIG-303602 from the European Commission, and from Elkartek Grant No. KK-2016/00025. D.V. acknowledges support from NSF Grant DMR-1408838 and thanks J. Bonini for useful discussions.

Appendix A: Level repulsion versus level crossing at generic points on a rotation axis

Let $|u\rangle$ and $|v\rangle$ be two distinct eigenstates of the screw symmetry operator C_{n_m} at a generic point K_z along the rotation axis of Eq. (2), and let α_{p_u} and α_{p_v} be the corresponding eigenvalues given by Eq. (6). Suppose the two states are also degenerate eigenstates of the Hamiltonian H, which by assumption commutes with C_{n_m}. Now add a small perturbation ΔH that respects the C_{n_m} symmetry. We want to know the conditions under which ΔH can couple the two states and open a gap. If the crossing can be removed in this way then it means that the original Hamiltonian H was fine-tuned.

The coupling matrix element is

$$\begin{aligned}\langle v|\Delta H|u\rangle &= \langle v|C_{n_m}^{-1}\left(C_{n_m}\Delta H C_{n_m}^{-1}\right)C_{n_m}|u\rangle \\ &= e^{i2\pi(p_u-p_v)/n}\langle v|\Delta H|u\rangle, \qquad \text{(A1)}\end{aligned}$$

where we used $[\Delta H, C_{n_m}] = 0$. There are two cases:

1. If $p_u \neq p_v \mod n$ Eq. (A1) can only be satisfied with $\langle v|\Delta H|u\rangle = 0$, which means that the perturbation does not open a gap: The crossing is robust against symmetry-preserving perturbations.
2. If $p_u = p_v \mod n$ then $\langle v|\Delta H|u\rangle$ can be nonzero, and ΔH will generically split the degeneracy.

Appendix B: Details of the numerical calculations

1. Ground state calculations

The electronic structure calculations of Secs. III and V were carried out within the framework of density-functional theory, as implemented in the `VASP` code package [28, 29]. This code uses a plane-wave basis set to expand the valence wave functions, and the projector-augmented wave method to describe the core-valence interaction [30, 31]. Except for Sec. V A, the calculations reported in this work include spin-orbit coupling in the core-valence interaction.

Fully-relativistic total energy calculations for hcp Co in its ferromagnetic ground state were carried out using the experimental lattice parameters $a = 2.506$ Å and $c = 4.067$ Å [32]. Exchange and correlation effects were treated using the Perdew, Burke, and Ernzerhof generalized-gradient approximation [33].

For the calculations on trigonal Te we used the experimental parameters $a = 4.458$ Å and $c = 5.925$ Å [34], and a relaxed value of $u = 0.274$ for the dimensionless helix parameter [24], which differs slightly from the experimental value of $u = 0.255$ [34]. Both the generalized-gradient approximation and the local-density approximation incorrectly predict a semi-metallic rather than semiconducting ground state for this material, due to a closing of the gap at the H point. Although this issue does not greatly affect our study of degeneracies along the ΓA line, we have opted to correct it by using instead the so-called HSE06 hybrid functional [35]. In this way we obtained an energy gap of 0.312 eV at H from a fully-relativistic calculation, in good agreement with both the calculated value of 0.314 eV obtained using the GW method [11] and the experimental value of 0.323 eV [36].

2. Post-processing using a Wannier-function basis

In order to interpolate the energy bands and calculate the chiral charges of the Weyl nodes, we use the formalism of maximally-localized Wannier functions [37, 38] as implemented in the `Wannier90` code package [39, 40].

Exploring the bandstructure of hcp Co over the BZ we find that the bands shown in Fig. 1 cross with higher-lying bands [17], and thus we use the disentanglement procedure [38] to construct the Wannier functions. The trial orbitals are chosen to be sp^3 hybrids and atom-centered d orbitals, totaling nine Wannier functions per

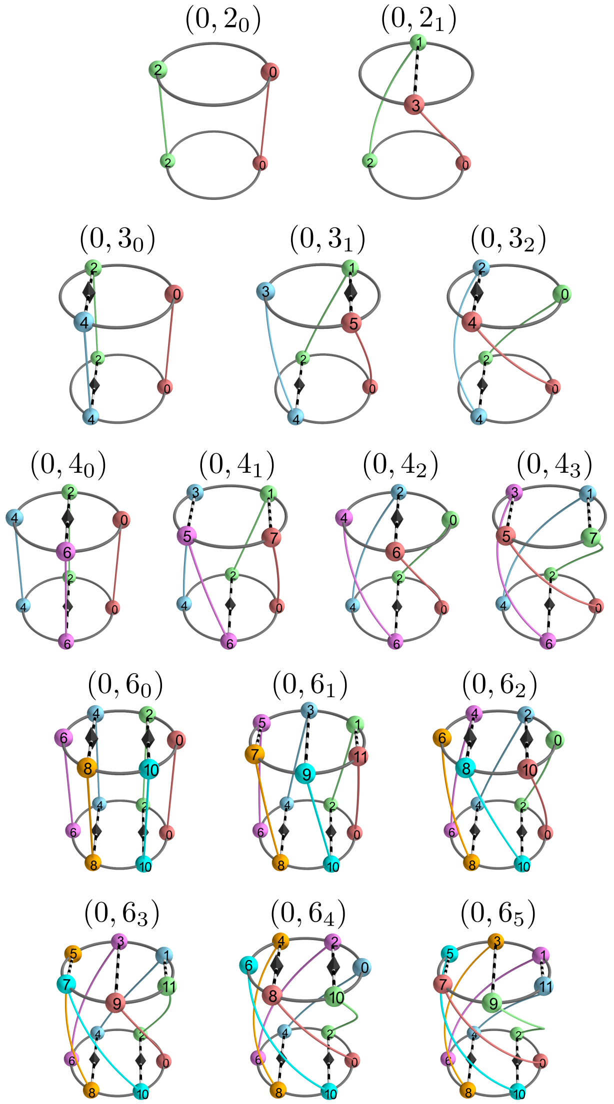

FIG. 7. (Color online) Schematic representation of the types of degeneracies protected by $\mathcal{T}$ and n_m symmetry at the TRIM $K_z = 0$ and π along an n_m-invariant axis $(0, 0, K_z)$ in the BZ. Each diagram is labeled by (F, n_m), and here we show the diagrams for spinless $\mathcal{T}$ ($F = 0$) and all n_m symmetries compatible with lattice periodicity. For a detailed explanation, see the captions of Figs. 2 and 3.

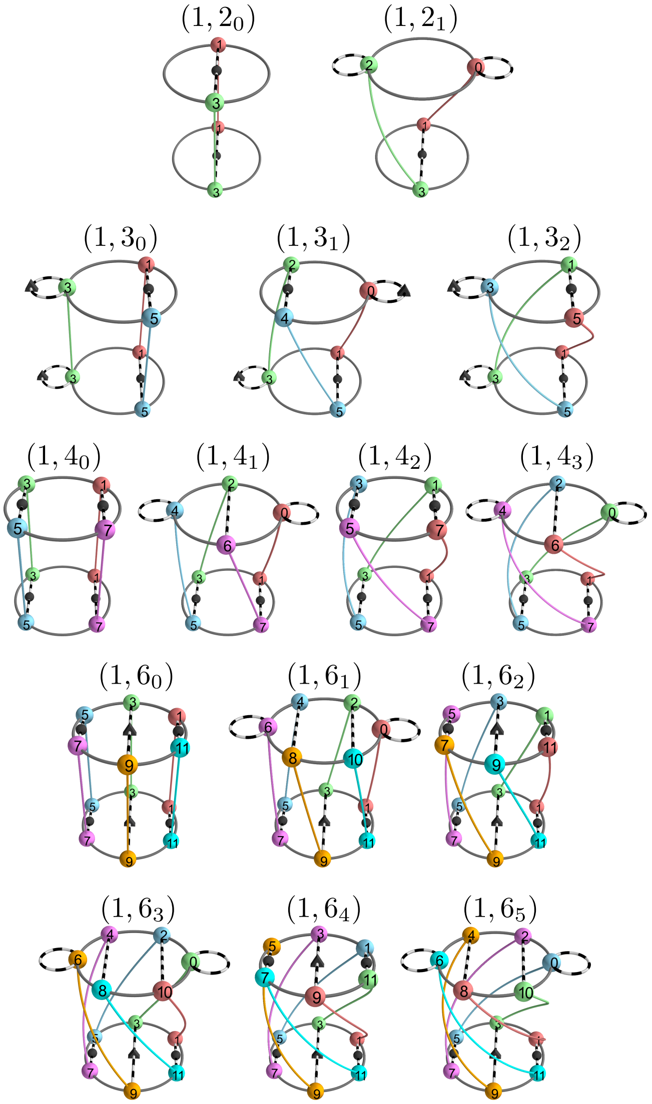

FIG. 8. (Color online) Same as Fig. 7, but for spinful $\mathcal{T}$ ($F = 1$).

atom and spin channel. The outer energy window [38] spans the range from −20 eV to +70 eV relative to the Fermi level, which covers all $4s$, $4p$ and $3d$ states present in the pseudopotential calculation, while the frozen energy window [38] goes from −20 eV to +7 eV.

The $5p$ bands of trigonal Te are well separated from the lower $5s$ states, and they cross with higher-lying sates only in a small region of the BZ. The outer energy window goes from −8 eV to +5 eV relative to the valence-band maximum, the inner frozen window from −8 eV to +2.5 eV, and we use atom-centered p-type trial orbitals for the initial projections. The resulting Wannier functions are similar to those obtained in Ref. [11] for the same material.

The chiral charges are calculated from the quantized Berry-curvature flux through small surfaces enclosing the individual Weyl nodes [10],

$$\chi_{l\alpha} = \frac{1}{2\pi} \oint_S dS\, \hat{\boldsymbol{n}} \cdot \boldsymbol{\Omega}_l(\boldsymbol{k}) \tag{B1a}$$

$$\boldsymbol{\Omega}_l(\boldsymbol{k}) = i\langle \boldsymbol{\nabla}_{\boldsymbol{k}} u_{l\boldsymbol{k}} | \times | \boldsymbol{\nabla}_{\boldsymbol{k}} u_{l\boldsymbol{k}} \rangle. \tag{B1b}$$

Here $\hat{\boldsymbol{n}}$ is the unit surface normal pointing outwards, and l is the lower of the two bands that cross. In practice the Berry curvature $\boldsymbol{\Omega}_n(\boldsymbol{k})$ is evaluated on a dense grid of k points by Wannier interpolation [41], and we choose the closed surface S to be a parallelepiped with the α-th Weyl node between bands l and $l+1$ at the center [10].

Appendix C: Diagrams describing the types of degeneracies at TRIM on a rotation axis

We present here the complete set of (F, n_m) diagrams introduced in Sec. IV B to describe the degeneracies occurring at TRIM on a rotation axis, assuming no other symmetries are present. The allowed degeneracies are Weyl points with chiral charges of magnitude $|\chi| = 1, 2$ or 3, and band glueing extending over the entire BZ face orthogonal to the symmetry axis. Figure 7 contains the diagrams for spinless $\mathcal{T}$ $(F = 0)$, and Fig. 8 contains the diagrams for spinful $\mathcal{T}$ $(F = 1)$.

The magnitude of the chiral charge has a simple interpretation in terms of these diagrams: When $F = 0$ $(F = 1)$, $|\chi|$ is equal to the smallest nonzero even (odd) number of hops around the unit circle needed to travel between spheres connected by a dashed line or loop with a marker. It follows that $|\chi|$ must be even when $F = 0$, and odd when $F = 1$. For $n = 2, 3, 4, 6$, the only possible values are $|\chi| = 2$ for $F = 0$ and $|\chi| = 1, 3$ for $F = 1$, with $|\chi| = 3$ requiring $n = 3$ or 6, in agreement with Tables II and III.

Appendix D: Valence and low-lying conductions bands of trigonal Te

We saw in Sec. V A that the spinless band structure of Te consists of 3-band complexes with topologically-required contact points along the 3-fold axis ΓA. In addition to the double Weyl nodes pinned to Γ and A by $\mathcal{T}$ symmetry, there was an additional Weyl crossing between Γ and A in the complex of Fig. 4. This degeneracy is accidental, and can be eliminated by changing the Hamiltonian without changing the symmetry [5]. This is corroborated by Fig. 9(a), where two more band complexes are shown. Both have double Weyl nodes at Γ and A, but the topmost valence complex contains no accidental crossings in between. In this scenario with minimal connectivity the double nodes at Γ and A must have opposite chiralities, as can be seen from Table II.

Figure 9(b) shows the spinful bands for the same three band complexes. The ordering in energy of the single and triple nodes at Γ and/or A is different in the three complexes, but the rules of the $(1, 3_1)$ diagram of Fig. 2(b) for hooking up the states are such that one necessarily ends up with the six bands forming a connected group in the sense of Ref. [5].

One noteworthy difference with respect to the spinless case of Fig. 9(a) is that it is not possible to eliminate all the Weyl nodes between Γ and A. The minimum number of such crossings per 6-band complex is two, and it requires that at both TRIM the triple node lies in energy between the two single nodes; the two unremovable unpinned crossings then occur between the red and green branches. This scenario is almost realized in the upper complex shown in Fig. 9(b), except for an additional accidental crossing between the two lowest bands. Crossings that “can be moved but not removed” while preserving the symmetry of the Hamiltonian were first discussed in Refs. [42, 43].

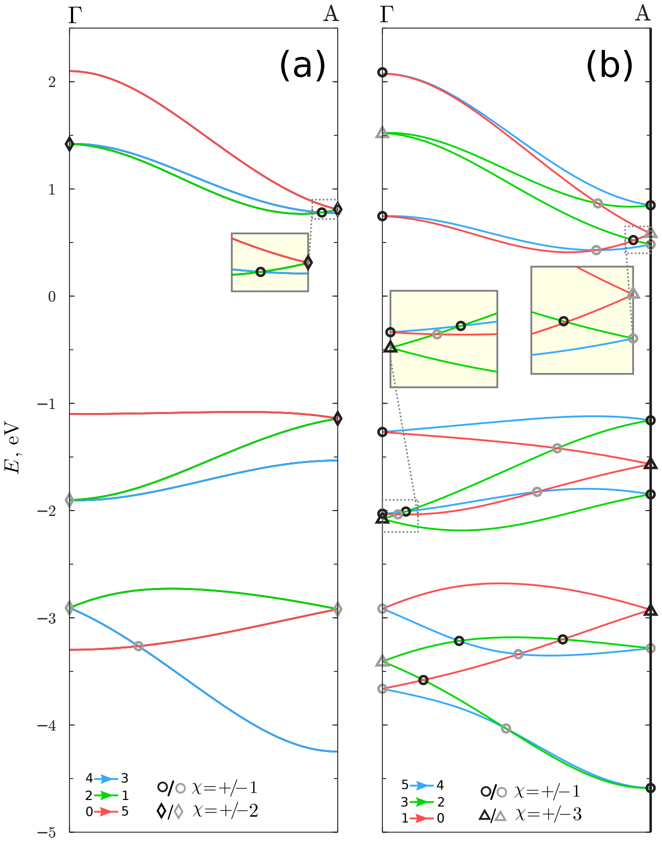

FIG. 9. Three complexes (two valence and one conduction) in the band structure of Te, plotted along the 3-fold axis ΓA with energies measured from the valence-band maximum. The bands in panels (a) and (b) were calculated without and with spin-orbit coupling, respectively. The meaning of the colors and markers is the same as in Figs. 4 and 5(a), which focus on the valence complex shown here at the bottom.

Appendix E: Effect of two-fold rotational symmetry on the Zeeman splitting of triple Weyl nodes in Te

The point group of trigonal Te contains a pure 2-fold rotation operation [24, 25] that leaves invariant the points Γ and A where triple Weyl nodes occur (the invariant lines are ΓK and AH). That 2_0 symmetry was not taken into account when analyzing in Sec. V C the splitting of a triple node by a Zeeman field. In this Appendix we show that its presence pins the three single nodes that split from the triple node to the ΓMLA planes in the BZ.

To proceed we need to find the constraints imposed by the 2_0 symmetry on the unperturbed effective Hamiltonian of a triple node. The first step is to write down the matrix C_{2_0} representing the 2_0 operation in the basis of the two states forming the triple node. Since that operation sends K_z into $-K_z$ and the function $g(0,0,q_z)$ multiplying σ_z in $H_{\rm eff}(0,0,K_z+q_z)$ is odd [see Eq. (18)], it follows that the basis states transform one into the other with some phase factors,

$$C_{2_0} = \begin{pmatrix} 0 & e^{i\phi_2} \\ e^{i\phi_1} & 0 \end{pmatrix}. \tag{E1}$$

From $(2_0)^2 = (-1)^F$ we obtain for spinful electrons the constrain $e^{i(\phi_1+\phi_2)} = -1$, while $\phi_1 - \phi_2$ depends on the arbitrary choice of phases for the two basis states. Since we have not fixed those phases anywhere so far we are free to choose $\phi_1 = \phi_2 = -\pi/2$, leading to

$$C_{2_0} = -i\sigma_x. \tag{E2}$$

The 2_0 operation transforms the wavevector measured relative to the nodal point Γ or A as $q_+ \leftrightarrow q_-$ and $q_z \to -q_z$, and using Eq. (1) we find as the invariance condition for the unperturbed effective Hamiltonian $C_{2_0} H_{\rm eff}(q_+,q_-,q_z)C_{2_0}^{-1} = H_{\rm eff}(q_-,q_+,-q_z)$. Inserting Eq. (3) for $H_{\rm eff}$ in this relation and using Eq. (E2) leads to the constraints

$$f(q_-,q_+,-q_z) = f^*(q_+,q_-,q_z) \tag{E3a}$$

$$g(q_-,q_+,-q_z) = -g(q_+,q_-,q_z) \tag{E3b}$$

which imply, for the expansion coefficients in Eq. (4),

$$A_{n_1n_2n_3} = (-1)^{n_3} A^*_{n_1n_2n_3} \tag{E4a}$$

$$B_{m_1m_2m_3} = (-1)^{m_3+1} B_{m_2m_1m_3}. \tag{E4b}$$

It follows from the first condition that $A_{n_1n_2n_3}$ is real (purely imaginary) when n_3 is even (odd), and from the second combined with Eq. (5) that $B_{m_1m_2m_3}$ is real (purely imaginary) when m_3 is odd (even).

When applied to the unperturbed effective Hamiltonian of a triple Weyl node in trigonal Te [Eq. (24) with $M_z = 0$], the above constraints from 2_0 symmetry imply that the parameters $\alpha = B_{001}$, $a = A_{300}$ and $b = A_{030}$ are real, while $c = B_{300}$ and $\beta = A_{001}$ are purely imaginary. As a result the previously complex quantities $\widetilde{a}$ and $\widetilde{b}$ appearing in Eq. (27) have now become real, and $\widetilde{\gamma}$ has become purely imaginary. The latter follows from the fact that 2_0 symmetry renders γ purely imaginary:

$$\begin{aligned}\gamma &= \langle u|\tau_z|v\rangle = \langle C_{2_0}u|C_{2_0}\tau_z C_{2_0}^{-1}|C_{2_0}v\rangle \\ &= -\langle v|\tau_z|u\rangle = -\gamma^*,\end{aligned} \tag{E5}$$

where $C_{2_0}|v\rangle = -i|u\rangle$ and $C_{2_0}|u\rangle = -i|v\rangle$ according to Eq. (E2), and $C_{2_0}\tau_z C_{2_0}^{-1} = -\tau_z$ according to the algebra for spin-$\frac{1}{2}$ rotations [21]. Under these circumstances the real part of Eq. (27) reduces to $(\widetilde{a}+\widetilde{b})\cos(3\phi) = 0$, which for $\widetilde{a} \neq -\widetilde{b}$ has six inequivalent roots

$$\phi = \frac{\pi}{6} + l\frac{\pi}{3}, \quad l = 0,1,\ldots,5, \tag{E6}$$

and from the imaginary part of Eq. (27) we find, using $\sin(3\phi) = (-1)^l$,

$$q_\perp^3 = (-1)^l \frac{M_z {\rm Im}[\widetilde{\gamma}]}{\widetilde{b}-\widetilde{a}}. \tag{E7}$$

Depending on the various parameters, the three physical solutions with a positive $q_\perp$ are the ones with either even or odd values of l. These two possibilities realize the two types of 3-fold symmetric patterns where the split Weyl nodes lie on the ΓMLA planes.

---

[1] L. P. Bouckaert, R. Smoluchowski, and E. Wigner, "Theory of Brillouin Zones and Symmetry Properties of Wave Functions in Crystals," Phys. Rev. **50**, 58 (1936).

[2] Conyers Herring, "Effect of Time-Reversal Symmetry on Energy Bands of Crystals," Phys. Rev. **52**, 361 (1937).

[3] C. Herring, "Accidental Degeneracy in the Energy Bands of Crystals," Phys. Rev. **52**, 365 (1937).

[4] H. B. Nielsen and M. Ninomiya, "Absence of neutrinos on a lattice," Nucl. Phys. B **185**, 20 (1981).

[5] L. Michel and J. Zak, "Connectivity of energy bands in crystals," Phys. Rev. B **59**, 5998 (1999).

[6] A. M. Turner and A. Vishwanath, "Beyond Band Insulators: Topology of Semimetals and Interacting Phases," in *Topological Insulators* (Elsevier, Amsterdam, 2013) Chap. 11, p. 293.

[7] C. Fang, M. J. Gilbert, X. Dai, and B. A. Bernevig, "Multi-Weyl Topological Semimetals Stabilized by Point Group Symmetry," Phys. Rev. Lett. **108**, 266802 (2012).

[8] J. L. Mañes, "Existence of bulk chiral fermions and crystal symmetry," Phys. Rev. B **85**, 155118 (2012).

[9] L. Lu, J. D. Joannopoulos, and M. Soljačić, "Topological photonics," Nature Photon. **8**, 821 (2014).

[10] D. Gosálbez-Martínez, I. Souza, and D. Vanderbilt, "Chiral degeneracies and Fermi-surface Chern numbers in bcc Fe," Phys. Rev. B **92**, 085138 (2015).

[11] M. Hirayama, R. Okugawa, S. Ishibashi, S. Murakami, and T. Miyake, "Weyl Node and Spin Texture in Trigonal Tellurium and Selenium," Phys. Rev. Lett. **114**, 206401 (2015).

[12] K. Nakayama, M. Kuno, K. Yamauchi, S. Souma, K. Sugawara, T. Oguchi, T. Sato, and T. Takahashi, "Band splitting and Weyl nodes in trigonal tellurium studied by angle-resolved photoemission spectroscopy and density functional theory," Phys. Rev. B **95**, 125204 (2017).

[13] H. Weng, C. Fang, Z. Fang, B. A. Bernevig, and X. Dai, "Weyl Semimetal Phase in Noncentrosymmetric Transition-Metal Monophosphides," Phys. Rev. X **5**, 011029 (2015).

[14] S.-M. Huang, S.-Y. Xu, I. Belopolski, C.-C. Lee, G. Chang, B. Wang, N. Alidoust, G. Bian, M. Neupane, C. Zhang, S. Jia, A. Bansil, H. Lin, and M. Z. Hasan, "A Weyl Fermion semimetal with surface Fermi arcs in

the transition metal monopnictide TaAs class," Nature Commun. **6**, 7373 (2015).

[15] In Ref. [7], the opposite choice was made, i.e., $B_{001} < 0$ in Eq. (10). As a result, the chiral charges in Table I of that work have the opposite signs compared to our Table I.

[16] M. J. Buerger, *Elementary Crystallography* (Wiley, New York, 1956).

[17] G. J. McMullan, D. D. Pilgram, and A. Marshall, "Fermi surface and band structure of ferromagnetic cobalt," Phys. Rev. B **46**, 3789 (1992).

[18] W.-J. Chen, M. Xiao, and C. T. Chan, "Photonic crystals possessing multiple Weyl points and the experimental observation of robust surface states," Nature Commun. **7**, 13038 (2016).

[19] Consider a crystal with n_m symmetry. For $n = 3$ the TRIM that do not project onto $\overline{\Gamma}$ on the projected 2D BZ are at the three $\overline{\mathrm{M}}$ points, while the 3-fold axes in k space are at $\overline{\mathrm{K}}$ and $\overline{\mathrm{K}'}$, so there are no TRIM on a 3-fold axis except at $\overline{\Gamma}$. For $n = 6$ there are no 6-fold axes off $\overline{\Gamma}$, only 3-fold axes at $\overline{\mathrm{K}}$ and $\overline{\mathrm{K}'}$ which do not contain TRIM, and 2-fold axes at $\overline{\mathrm{M}}$, $\overline{\mathrm{M}}'$, and $\overline{\mathrm{M}}''$. Thus, 3-fold and 6-fold axes never contain TRIM except at $\overline{\Gamma}$.

[20] The degeneracy follows from Eq. (17), which at the TRIM becomes $[\mathcal{T}, H(\boldsymbol{k})] = 0$.

[21] J. J. Sakurai, *Modern Quantum Mechanics* (Addison-Wesley, Reading, Massachussetts, 1994).

[22] V. Heine, *Group Theory in Quantum Mechanics* (Pergamon Press, New York, 1960).

[23] G. Chang, D. S. Sanchez, B. J. Wieder, S.-Y. Xu, F. Schindler, I. Belopski, S.-M. Huang, B. Singh, D. Wu, T. Neupert, T.-R. Chang, H. Lin, and M. Z. Hasan, "Kramers theorem-enforced Weyl fermions: Theory and Materials Predictions (Ag_3BO_3, $TlTe_2O_6$ and Ag_2Se related families)," arXiv:1611.07925 (2016).

[24] R. H. Asendorf, "Space group of tellurium and selenium," J. Chem. Phys. **27**, 11 (1957).

[25] A. Nussbaum, "Group Theory and the Energy Band Structure of Semiconductors," Proc. IRE **50**, 1762 (1962).

[26] K. Natori, "Band Theory of the Optical Activity of Crystals," J. Phys. Soc. Japan **39**, 1013 (1975).

[27] `https://en.wikipedia.org/wiki/Rock-paper-scissors`.

[28] G. Kresse and J. Hafner, "Ab initio molecular dynamics for open-shell transition metals," Phys. Rev. B **48**, 13115 (1993).

[29] G. Kresse and J. Furthmüller, "Efficiency of ab-initio total energy calculations for metals and semiconductors using a plane-wave basis set," Comput. Mater. Sci. **6**, 15 (1996).

[30] P. E. Blöchl, "Projector augmented-wave method," Phys. Rev. B **50**, 17953 (1994).

[31] G. Kresse and D. Joubert, "From ultrasoft pseudopotentials to the projector augmented-wave method," Phys. Rev. B **59**, 1758 (1999).

[32] H. Masumoto, K. Watanabe, and K. Inagawa, "Magnetic Properties of Hexagonal Close-Packed Structure Type Co–Ir Binary Alloys," Trans. Jpn. Inst. Met. **17**, 592 (1976).

[33] J. P. Perdew, K. Burke, and M. Ernzerhof, "Generalized gradient approximation made simple," Phys. Rev. Lett. **77**, 3865 (1996).

[34] N. Bouad, L. Chapon, R.-M. Marin-Ayral, F. Bouree-Vigneron, and J.-C. Tedenac, "Neutron powder diffraction study of strain and crystallite size in mechanically alloyed PbTe," J. Solid State Chem. **173**, 189 (2003).

[35] J. Paier, M. Marsman, K. Hummer, G. Kresse, I. C. Gerber, and J. G. Angyán, "Screened hybrid density functionals applied to solids," J. Chem. Phys. **124**, 154709 (2006).

[36] V. B. Anzin, M. I. Eremets, Y. V. Kosichkin, A. I. Nadezhdinskii, and A. M. Shirokov, "Measurement of the energy gap in tellurium under pressure," Phys. Status Solidi A **42**, 385 (1977).

[37] N. Marzari and D. Vanderbilt, "Maximally localized generalized Wannier functions for composite energy bands," Phys. Rev. B **56**, 12847 (1997).

[38] I. Souza, N. Marzari, and D. Vanderbilt, "Maximally localized Wannier functions for entangled energy bands," Phys. Rev. B **65**, 035109 (2001).

[39] A. A. Mostofi, J. R. Yates, Y.-S. Lee, I. Souza, D. Vanderbilt, and N. Marzari, "wannier90: A tool for obtaining maximally-localised Wannier functions," Comput. Phys. Commun. **178**, 685 (2008).

[40] A. A. Mostofi, J. R. Yates, G. Pizzi, Y.-S. Lee, I. Souza, D. Vanderbilt, and N. Marzari, "An updated version of wannier90: A tool for obtaining maximally-localised Wannier functions," Comput. Phys. Commun. **185**, 2309 (2014).

[41] X. Wang, J. R. Yates, I. Souza, and D. Vanderbilt, "*Ab initio* calculation of the anomalous Hall conductivity by Wannier interpolation," Phys. Rev. B **74**, 195118 (2006).

[42] L. Michel and J. Zak, "Elementary energy bands in crystalline solids," Europhys. Lett. **50**, 519 (2000).

[43] J Zak, "Topologically unavoidable points and lines of crossings in the band structure of solids," J. Phys. A: Math. Gen. **35**, 6509 (2002).